Progress In Electromagnetics Research C, Vol. 136, 37–50, 2023

Miniaturized Low-Loss Band Pass Filter Based on Coupling Effect of Defective Structures for Ultra Broad Band Applications

Mani Divya Shree and Inabathini Srinivasa Rao*

Abstract—In this paper, a compact, symmetric, simple, and highly selective Ultra Broad Band (UBB) Band Pass Filter (BPF) is constructed on a low-loss Taconic dielectric substrate. The top layer of the BPF is loaded with three headphone-shaped Defected Microstrip Structures (DMSs) and four Open Circuit (OC) stubs whereas the bottom layer is etched with three star-shaped Defected Ground Structures (DGSs). The proposed BPF is designed and simulated using High-Frequency Structure Simulator (HFSS) software at f_0. The proposed BPF shows 20 dB return loss and 0.4 dB insertion loss in the 3 dB passband covering 0.52 GHz to 17.1 GHz owing to 16.58 GHz Band Width (BW). Additionally, 10 dB and 25 dB upper stopband rejection is achieved with 1.3 GHz and 1 GHz BW, respectively. Maximum group delay of the simulated filter is about 2.95 ns. The fabricated model transmits from 0.8 GHz to 17.4 GHz which in turn offers a 16.6 GHz BW at 3 dB level. The reflection coefficient of the fabricated filter is about −18 dB, and insertion loss varies from 0 dB to 0.72 dB inside the Transmission Band (TB) with a Fractional Band Width (FBW) of 178.5% and 3.35 ns maximum group delay. Moreover, the occurrence of Transmission Zeroes (TZs) and Reflection Poles (RPs) make the filter highly selective and low loss (flatness). The measured results agree with the simulated outputs with slight deviations due to fabrication tolerances and connector loss. The size of the filter is $0.36\lambda_g * 0.36\lambda_g$. Thus the proposed filter is suitable for mobile phones and satellite communication applications approximately covering L, S, C, X, and Ku frequency bands.

1. INTRODUCTION

Microwave Band Pass Filter (BPF) plays a significant role in the field of communications. The design of a wide band filter is more complex than that of a narrow BPF as it must meet the requirements such as wide Band Width (BW), compact size, low insertion loss, and sharp roll-off. Resonators, inductive stubs, and capacitive gaps with and without periodic unit cells are used in combination to reduce the size and improve the frequency response of BPFs. Various resonator techniques have been implemented in the design of BPFs to optimize at least one of the filter characteristics [1–5]. In [6], BPF is constructed by using coupled line resonators, and in conjunction with that, a larger stopband feature is accomplished by implementing the concept of Defected Ground Structure (DGS). The combination of ring resonators on the top layer and modified defects on the ground layer results in a miniaturized BPF [7–9]. The addition of various defective ground structures to the bottom layer of a BPF yields wideband response and enhanced stopband characteristics [10–12]. To enhance the frequency response of a BPF, researchers have focused on the low loss performance and designed BPFs using a variety of techniques [13–16]. From the survey, we found that lower number of works were carried out on BPFs with wider BW especially using DMS and DGS structures.

In this work, a low-loss and miniaturized BPF for Ultra Broad Band (UBB) applications is proposed. The compactness and BW (for UBB) are achieved using a Defected Microstrip Structure (DMS) on the

Received 30 May 2023, Accepted 25 July 2023, Scheduled 10 August 2023
* Corresponding author: Inabathini Srinivasa Rao (israo@vit.ac.in).
The authors are with the School of Electronics Engineering, Vellore Institute of Technology, Vellore-632014, Tamil Nadu, India.

top layer and DGS at the bottom layer. The Open Circuited (OC) stubs on the top layer are responsible for the low-loss characteristic of the filter. To improve the filter properties, three pairs of DMS and DGS structures with the concept of coupling have been integrated into the filter. In addition to the transmission line analysis of the proposed filter, the equivalent circuit model of the filter is also simulated. The filter parameters are optimized for better performance by accomplishing parametric analysis. The novelty of the work lies in the innovative structure of DMS and DGS resonators in addition to via less concepts. Also, the properties of the filter are controlled by structural dimensions without using passive components like capacitors, diodes, and such devices. The proposed UBB BPF is realized for the verification of simulated and analytical results.

2. FILTER DESIGN AND SYNTHESIS

DMS is formed when planar microstrip lines are etched with different geometries. By introducing defects in a microstrip line, it is possible to generate the slow-wave effect that is the trajectory of the current waves (Electric and Magnetic fields) which are delayed to get a bandpass or bandstop response [17]. Moreover, by employing the concept of DMS, there is a rise in the electrical length, effective inductance, and effective capacitance, and the defects are created in the microstrip line without perturbing the ground plane. As a result, DMS can be used in microwave circuits where miniaturization is important. Three headphone-shaped DMSs are etched on a 50 Ω microstrip line as shown in Fig. 1(a). A delay in the current flow due to DMS in the microstrip line can be described by a factor called the Slow Wave Factor (SWF) [18]. The SWF is the ratio of propagation constant (β) to free space wavenumber (k_0) as in Eq. (1).

$$SWF = \frac{\beta}{k_0} \tag{1}$$

DGS refers to the removal of any section of the ground plane. DGS also explores the same features as DMS, such as the slow-wave effect, which in turn rejects or allows a particular frequency or a band of frequencies. Consequently, DGS can be utilized based on the frequency of interest, making it well-suited for compact microwave applications. DGS can be proven as an equivalent parallel LC circuit similar to DMS as it is the reciprocal of the transmission line where the metal part of the line acts as an inductor and the gap as a capacitor. An asterisk (eight-pole star) shaped defect on the ground plane is proposed in this work as DGS and is shown in Fig. 1(b), and the equivalent circuit of defects (DMS and DGS) is modeled as a parallel LC circuit and is shown in Fig. 1(c). The inductance and capacitance values of

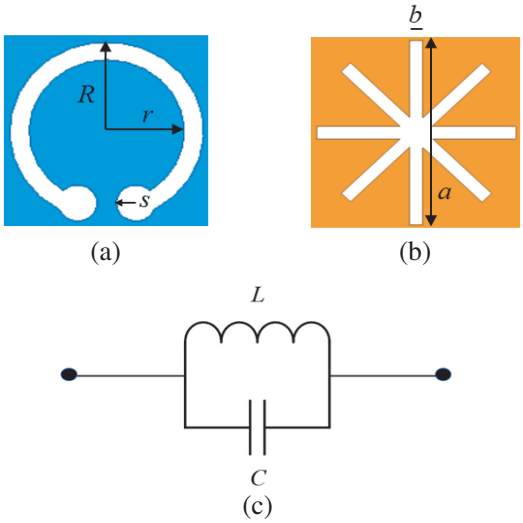

Figure 1. (a) Headphone-shaped DMS. (b) Star-shaped DGS. (c) Equivalent circuit model of DMS and DGS.

DMS and DGS can be computed from Eq. (2) and Eq. (3) [19] using the curve fitting method.

$$C = \frac{f_c}{200\pi(f_0^2 - f_c^2)} \quad F \tag{2}$$

$$L = \frac{1}{4\pi^2 f_0^2 C} \quad H \tag{3}$$

where $f_0 = \frac{1}{2\pi\sqrt{LC}}$ named as the resonant frequency of the resonator, and f_c is the 3 dB cut-off frequency of the resonator.

The top and bottom configurations of the proposed filter are shown in Fig. 2 and Fig. 3, respectively. On the top conducting layer, a 50 Ω microstrip line is designed at the center frequency ($f_0 = 7.5$ GHz) which acts as input and output feed lines. The top structure includes four OC stubs and three headphone-shaped DMSs. In the bottom conducting layer, three asterisk-shaped DGS resonators are etched. It is significant to observe that the axis of each DMS and DGS resonator is kept constant to achieve better coupling of electric and magnetic fields with compactness.

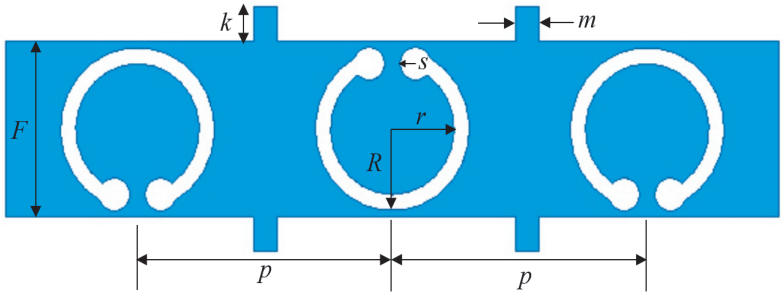

Figure 2. Top structure of proposed BPF.

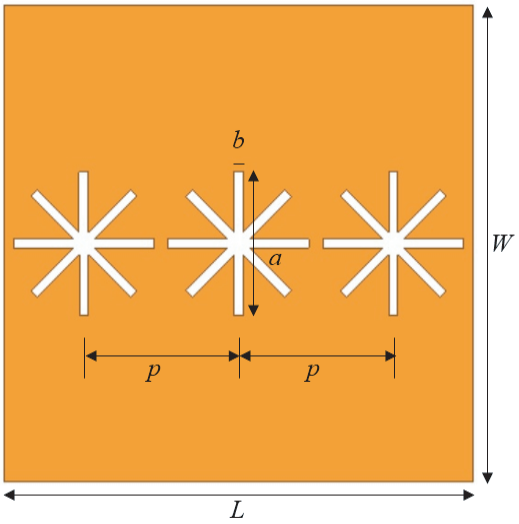

Figure 3. Bottom structure of proposed BPF.

Figure 4 shows the transmission line model of the top layer that holds transmission line, DMSs, and OC lines by employing stubs. In section **a**, the 50 Ω transmission line has equal width and length thereby providing an equal impedance (Z_0) and electrical length (θ_0) along the filter length. The impedance electrical length pair of the DMS resonator is (Z_{DM}, θ_{DM}). Since DMS is placed in the middle of transmission line section **a**, two transmission line sections arise before and after the DMS resonator

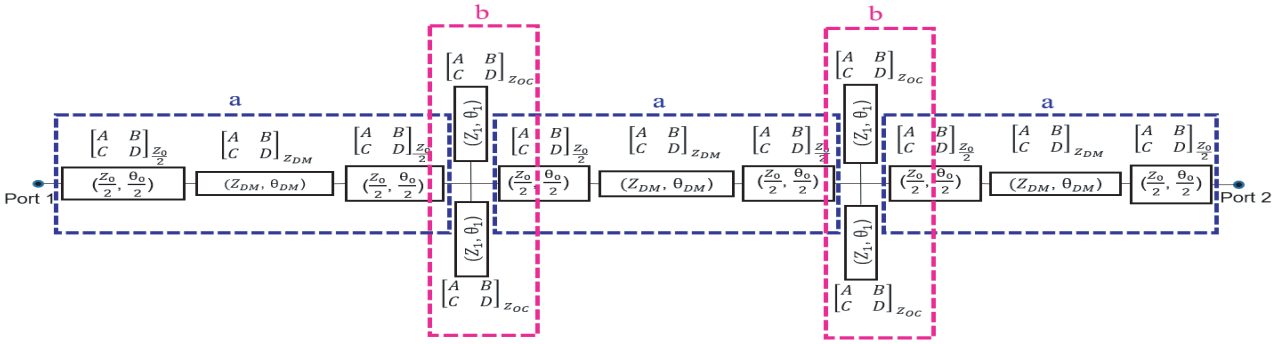

Figure 4. Top structure as stub representation.

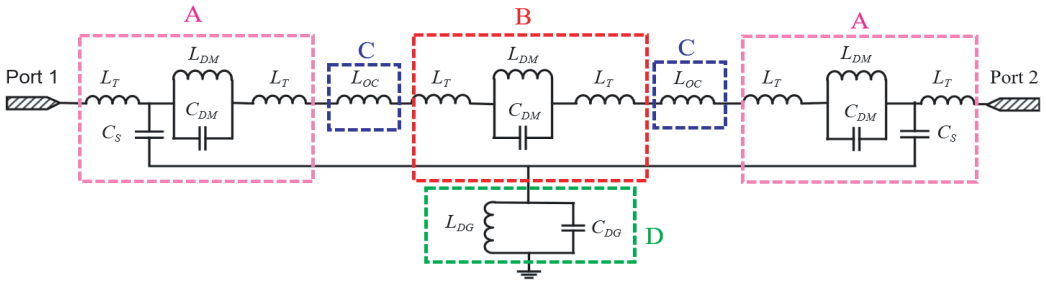

Figure 5. Equivalent circuit of proposed BPF.

with impedance electrical length pair $(\frac{Z_0}{2}, \frac{\theta_0}{2})$. Subsequently, section **b** is sandwiched between two section **a** with OC stubs. Impedance electrical length pair of OC stubs is denoted as (Z_1, θ_1). $ABCD$ matrices of the corresponding stubs in the top layer are depicted with corresponding subscripts.

The lumped element model of the proposed BPF is shown in Fig. 5. The transmission line along with the substrate (middle layer) is represented by a parallel inductor (L_T) and a series capacitor (C_S) whereas the DMS resonator can be modeled as a parallel LC circuit with L_{DM} as inductance and C_{DM} as capacitance. Similarly, the parallel connection of inductance (L_{DG}) and capacitance (C_{DG}) forms the DGS resonator. Depending on the length of the OC stub, the stub acts as an inductor denoted as L_{OC}. Portion **A** bears two half-section transmission lines and one DMS resonator with the substrate. Exclusion of substrate from portion **A** acts as portion **B** (one DMS and two half-section transmission lines). The OC stubs form portion **C** whereas section **D** has one parallel LC circuit which is the representation of three DGSs in the ground plane of the proposed filter. Finally, port 1 and port 2 with $50\,\Omega$ impedance match the transmission line impedance and excite the circuit.

The proposed BPF can be mathematically analyzed by the transmission line model using $ABCD$ matrix. The $ABCD$ matrix of half-section lossy transmission line $(\frac{TL}{2})$ is:

$$T_{\frac{TL}{2}} = \begin{bmatrix} A & B \\ C & D \end{bmatrix}_{\frac{TL}{2}} = \begin{bmatrix} \cos\theta_{\frac{L}{2}} & jZ_0 \sin\theta_{\frac{L}{2}} \\ \dfrac{j\sin\theta_{\frac{L}{2}}}{Z_0} & \cos\theta_{\frac{L}{2}} \end{bmatrix} \tag{4}$$

Using the data of half-section transmission line, the impedance and electrical length pair are found to be $(Z_{\frac{L}{2}}, \theta_{\frac{L}{2}}) = (50\,\Omega, 65^\circ)$ at centre frequency (f_0). By substituting the impedance and electrical length values in (4), the final $ABCD$ matrix of the half-section lossy transmission line is:

$$T_{\frac{TL}{2}} = \begin{bmatrix} -0.562 & j41.5 \\ j0.0166 & -0.562 \end{bmatrix} \tag{5}$$

From the dimensions of OC stubs, impedance and electrical lengths are obtained as: $(Z_{OC}, \theta_{OC}) = (127\,\Omega, 5.23^\circ)$. Eq. (6) provides the actual impedance of an OC stub:

$$Z_A = -jZ_{OC}\cot\theta_{OC} \tag{6}$$

After computation, Eq. (7) shows the actual OC stub impedance:

$$Z_A = -j1388\,\Omega \tag{7}$$

In general, the $ABCD$ matrix for a shunt stub is given by Eq. (8),

$$\begin{bmatrix} A & B \\ C & D \end{bmatrix}_{sh} = \begin{bmatrix} 1 & 0 \\ Y & 1 \end{bmatrix} \tag{8}$$

where $Y = \frac{1}{Z}$ is the admittance, and its reciprocal is termed as impedance (Z). Since the OC stubs are in parallel with the transmission line, the $ABCD$ matrix for the corresponding section is:

$$\begin{bmatrix} A & B \\ C & D \end{bmatrix}_{Z_{OC}} = \begin{bmatrix} 1 & 0 \\ Y_A & 1 \end{bmatrix} = \begin{bmatrix} 1 & 0 \\ \dfrac{1}{Z_A} & 1 \end{bmatrix} \tag{9}$$

Once the actual impedance is calculated, it is applied in Eq. (9):

$$T_{Z_{OC}} = \begin{bmatrix} A & B \\ C & D \end{bmatrix}_{Z_{OC}} = \begin{bmatrix} 1 & 0 \\ j0.000721 & 1 \end{bmatrix} \tag{10}$$

Equation (11) provides the impedance of DMS:

$$Z_{DMS} = \frac{1}{\dfrac{1}{j\omega L} + j\omega C} \tag{11}$$

The values of capacitance and inductance of the headphone-shaped DMS can be found using Eq. (2) and Eq. (3). By substituting the values of L and C in Eq. (11):

$$Z_{DMS} = -j4.6x10^{-3} \tag{12}$$

Since the DMSs are in series with half-section transmission lines, the $ABCD$ matrix can be:

$$T_{Z_{DMS}} = \begin{bmatrix} A & B \\ C & D \end{bmatrix}_{Z_{DMS}} = \begin{bmatrix} 1 & Z_{DMS} \\ 0 & 1 \end{bmatrix} = \begin{bmatrix} 1 & -j4.6x10^{-3} \\ 0 & 1 \end{bmatrix} \tag{13}$$

Equation (14) provides the final transmission line matrix of the top structure as:

$$T = T_{\frac{TL}{2}} * T^2_{Z_{OC}} * T^3_{Z_{DMS}} * T^2_{Z_{OC}} * T_{\frac{TL}{2}} \tag{14}$$

After substituting Eq. (5), Eq. (10), and Eq. (13) in Eq. (14), the final $ABCD$ matrix can be achieved as:

$$T = \begin{bmatrix} A & B \\ C & D \end{bmatrix} = \begin{bmatrix} -0.3058 & -j51.6147 \\ -j0.0177 & -0.3058 \end{bmatrix} \tag{15}$$

Hence, the elements of the $ABCD$ matrix are $A = -0.3058$, $B = -j51.6147$, $C = -j0.0177$, and $D = -0.3058$. Indeed, the values of insertion loss and return loss can be evaluated from Eq. (16) and Eq. (17) in terms of A, B, C, and D.

$$S_{11} = \frac{A + \dfrac{B}{Z_0} - CZ_0 - D}{A + \dfrac{B}{Z_0} + CZ_0 + D} = 0.0697 + j0.0222 \tag{16}$$

$$S_{21} = \frac{2}{A + \dfrac{B}{Z_0} + CZ_0 + D} = -0.3020 + j0.9468 \tag{17}$$

Therefore,

Return loss:

$$|S_{11}| = 0.0732;\ S_{11}(\text{dB}) = -20\log(0.0732) = 22.7\,\text{dB},$$

Insertion loss:

$$|S_{21}| = 0.993 = -20\log(0.993) = 0.06\,\text{dB}.$$

Thus, Fig. 6 shows the response of the filter concerning the top structure in terms of return loss and insertion loss at f_0 which is verified theoretically and matches the simulated values approximately.

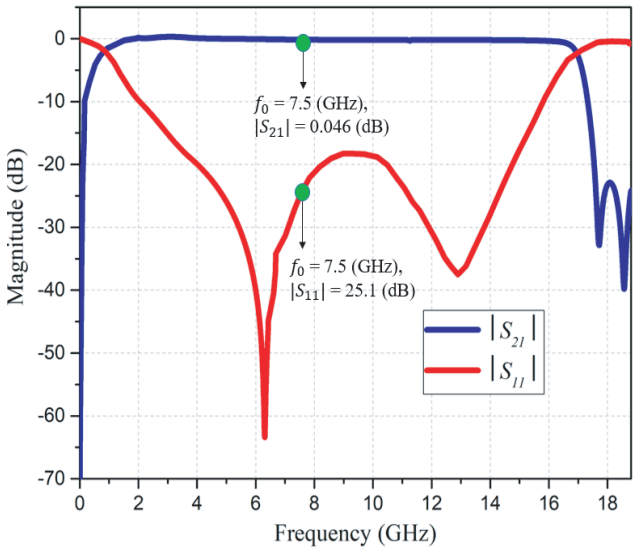

Figure 6. Response of top structure of filter at $f_0 = 7.5$ GHz.

3. COUPLING COEFFICIENT (M)

When two or more resonators are implemented on the metal layer, coupling occurs. In general, the effect of coupling is studied by fringing fields (electric or magnetic) and periodicity (p). Electric coupling, magnetic coupling, and mixed-coupling are three types of coupling associated with resonators. In the top layer of the proposed filter, three DMSs are etched with a periodicity (p) of 3.3 mm. The alternate arrangement of headphone-shaped DMSs offers mixed-coupling. The coupling coefficient between resonators is given by Eq. (18), where f_1 and f_2 are lower and higher resonant frequencies of DMS resonators, respectively, [20].

$$M = \frac{f_2^2 - f_1^2}{f_2^2 + f_1^2} \tag{18}$$

The periodicity is chosen based on filter length to reduce the system complexity and achieve compactness. As periodicity (p) varies from 2.1 mm to 3.5 mm, the coupling coefficient (M) drops from 0.83 to 0.01 linearly as seen in Fig. 7. Furthermore, it demonstrates that increased periodicity

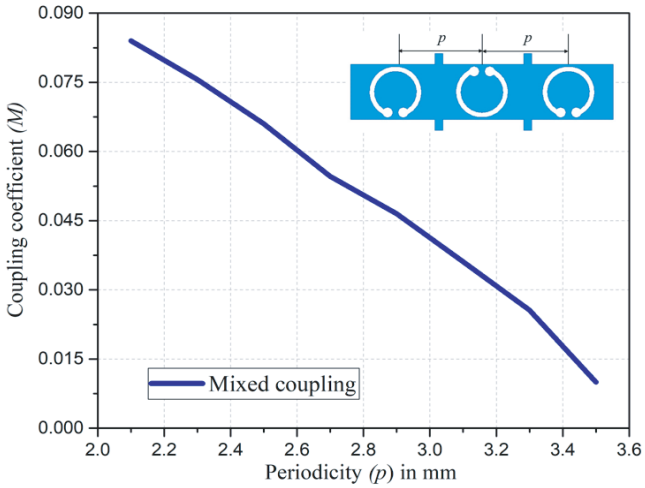

Figure 7. Correlation between periodicity (p) and coupling coefficient (M).

lowers the effect of coupling between DMS resonators.

In fact, the uniform periodicity of resonators has an influence on the attenuation level and BW of the stopband region [21]. In this work, when the distance between DMS resonators (p) is far, a reduction in the BW of the stopband is perceived. The attenuation level (depth of TZ) in the region of the stopband is higher for increased periodicity (p) between the DMS resonators. The periodicity (p) of star-shaped DGS resonators in the ground plane cannot be varied as it is compact due to its dimensions along the length of the filter. Three-unit cells of DMS and DGS are implanted in the proposed filter to increase the slow wave effect and achieve compactness [22] thereby realizing a UBB BPF. The reason behind placing the star-shaped DGS underneath the headphone-shaped DMS resonator is to accomplish a strong coupling of electric and magnetic fields among three layers and achieve a BPF that operates for UBB applications.

4. RESULTS AND DISCUSSION

The proposed BPF is designed and simulated using High-Frequency Structure Simulator (HFSS) software. The top layer is composed of a 50 Ω microstrip line, four OC stubs, and three headphone-shaped DMSs. The ground layer of the filter consists of three asterisk-shaped DGSs aligned with the three DMS of the top layer for coupling. The middle layer is a low-cost Taconic dielectric material (TLX-9) with a dielectric constant (ϵ_r) of 2.5 and a low dissipation factor of 0.0019. The top and bottom copper conducting layers are 0.035 mm thick, and the height of the middle substrate layer is 0.79 mm. The overall size of the BPF is $0.36\lambda_g * 0.36\lambda_g$ with three pairs of DMS and DGS resonators, and four OC stubs. Finally, input and output ports are excited by wave ports in HFSS along the z-axis. The design specifications are listed in Table 1 where λ_g is the guided wavelength calculated using the ratio of free space wavelength λ_0 (at f_0) to the square root of the effective dielectric constant (ϵ_{ref}).

Table 1. Dimensions of proposed BPF parameters (Unit: mm)

Parameter	Label	Dimension
Filter length	L	$0.36\lambda_g$
Filter width	W	$0.36\lambda_g$
Microstrip feed width	F	2.2
Star-shaped DGS length	a	3
Star-shaped DGS width	b	0.2
DMS outer circle radius	R	1
DMS inner circle radius	r	0.8
DMS small circle radius	s	0.2
OC stub length	k	0.5

4.1. *S*-Parameter

The response of the proposed BPF in Electro-Magnetic (EM) simulation is shown in Fig. 8. The 50 Ω microstrip line and DMSs on the top layer are responsible for the generation of TZs on both sides of the passband at 0 GHz (f_{z1}) and 18 GHz (f_{z2}) which makes the filter highly selective. When three DMS resonators are placed with uniform periodicity (p), two TZs (18 GHz (f_{z2}) and (18.8 GHz) (f_{z3})) are generated due to mixed-coupling of electric and magnetic fields. The RPs at 7.5 GHz (f_{p1}), 14.8 GHz (f_{p2}), and 16.2 GHz (f_{p3}) in the passband occur mainly due to the OC stubs on the top layer and DGSs at the bottom layer. Thus, the existence of TZs provides excellent out-of-band rejection whereas RPs offer better flatness in the TB of the filter. The designed filter shows a reflection loss of 20 dB and an insertion loss from 0 dB to 0.4 dB in the desired passband of the proposed BPF. At 3 dB level, the TB is from 0.52 GHz to 17.1 GHz. In general, the reason behind the 3 dB level is to ensure a minimum of 50%

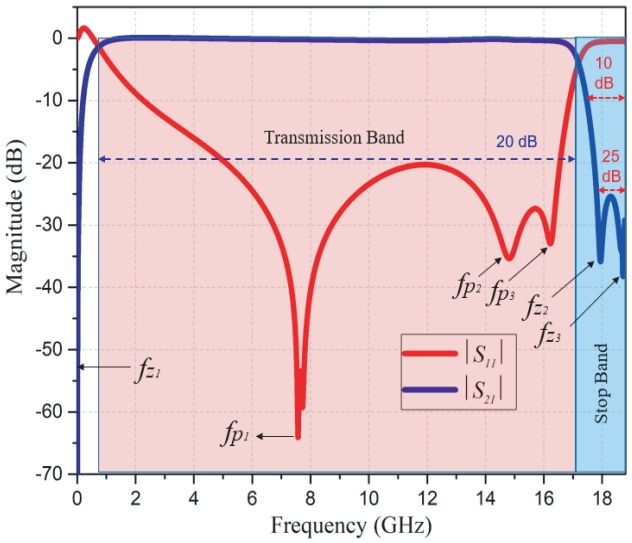

Figure 8. S-parameter plot of proposed BPF.

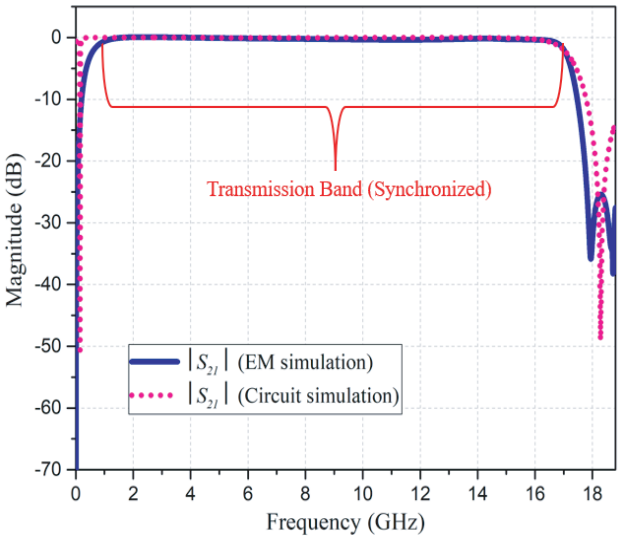

Figure 9. Comparison of proposed BPF performance in HFSS and Circuit simulation.

of the signal power transmitted in the TB of the filter. Furthermore, the upper stopband attenuation of the proposed BPF is about 10 dB from 17.5 GHz to 18.8 GHz resulting in 1.3 GHz BW. Additionally, 25 dB attenuation is attained from 17.8 GHz to 18.8 GHz with 1 GHz BW.

Using lumped elements, the proposed BPF is designed as a circuit and simulated. On observing Fig. 9, three TZs (f_{z1}, f_{z2}, and f_{z3}) are generated at 0 GHz, 18 GHz, and 18.8 GHz in HFSS software whereas in circuit simulation only two TZs (f_{z1}, and f_{z2}) are found at 0 GHz and 18.3 GHz, respectively. Moreover, TB covered by HFSS is 0 GHz to 17.1 GHz, and in circuit simulation, TB originates from 0.15 GHz to 17.2 GHz. Upper stopband rejection of 14.7 dB is seen from 18 GHz to 18.8 GHz in circuit simulation whereas 25 dB attenuation is achieved from 17.8 to 18.8 GHz in EM simulation. Hence, the synchronization of TB in EM simulation and circuit simulation of the proposed BPF is perceived.

4.2. Current Distribution

Additionally, the distribution of currents in vector form may be used to visualize the working mechanism of the designed BPF. The surface currents and their directions are shown by the arrowheads. The highest and lowest vector currents on the different surfaces are indicated by red and blue arrowheads. In Fig. 10(a), the surface currents in the microstrip feed travel forward and backward in a linear way with no interruption. Fig. 10(b) shows the ground plane current density plot where the arrowheads move straight in a to-and-fro motion without any perturbation, much as in feed. The currents in Fig. 10(c) move forward and backward in a nonlinear fashion due to the presence of stubs and headphone-shaped DMSs to create a long trajectory for the currents to travel and reach the other port.

Inside the first and last DMSs, the current flows in the counter-clockwise direction, and in the interior of the center DMS, the current flows in the clockwise direction. The difference in the current direction between DMSs is due to the alternate orientation of DMS resonators about 180°. The alternate orientation of DMS resonators leads to mixed-coupling which provides both electric and magnetic fringing fields at resonance. The maximum currents are concentrated in the corners of the microstrip feed line and along DMSs. In the bottom layer, the current moves in a backward direction and is delayed due to the manifestation of DGSs. Fig. 10(d) shows that the maximum to average currents in the bottom layer are concentrated in the region of DMS resonators due to the coupling between DMS and DGS resonators with dielectric material TLX-9. Three DMS and DGS resonators increase the slow wave effect and provide a better coupling which in turn produces a large BW for the UBB range.

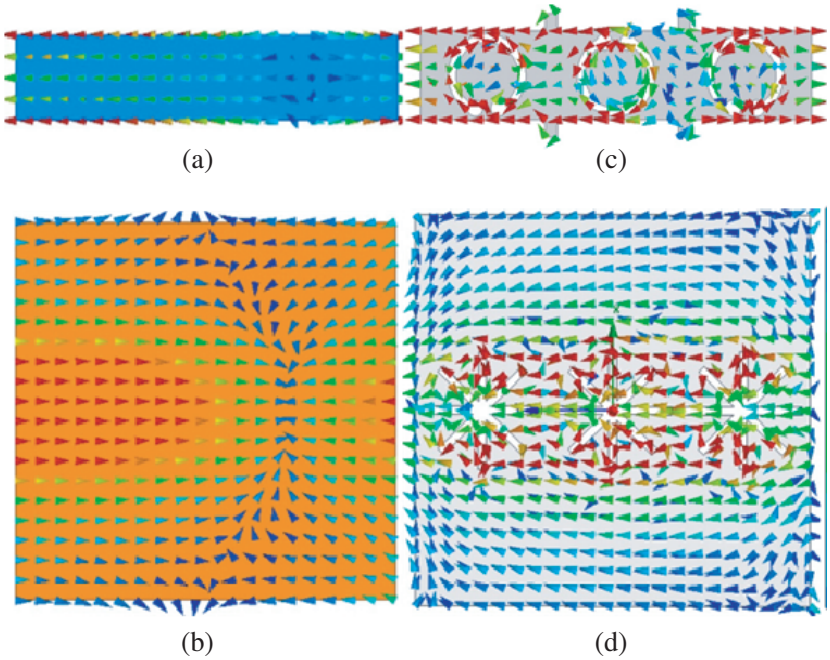

Figure 10. Surface current distribution at f_0 over (a) Unperturbed feed, (b) Unperturbed ground, (c) Top structure of filter, (d) Bottom structure of filter.

5. PARAMETRIC ANALYSIS

Parametric analysis is carried out in HFSS software to determine the influence of the design parameters on the proposed UBB filter as well as to fine-tune the filter for improved performance.

5.1. DGS Length (a) and DGS Width (b)

In the beginning, we experimented by varying the asterisk DGS length (a) from 1.5 mm to 3.5 mm with a 0.5 mm difference as shown in Fig. 11(a). Three RPs (f_{p1}, f_{p2}, and f_{p3}) almost shift towards higher frequencies for increasing ground resonator length (a). The amplitude of S_{11} decreases as the DGS length (a) increases. As a result, a has a significant influence on the return loss and the location of the RPs.

Similarly, change in the width of the DGS (b) from 0.2 mm to 1 mm is shown in Fig. 11(b). Here the return loss of the filter drops for the wider width of the DGS resonator. Additionally, the RP frequencies move towards higher frequencies thereby providing the right BW shift. Thus, the design parameter b is inversely proportional to the return loss feature of the proposed BPF.

5.2. DMS Inner Radius (r) and DMS Small Circle Radius (s)

The inner radius (r) of the headphone-shaped DMS is adjusted from 0.6 mm to 0.8 mm in 0.05 mm increments, as depicted in Fig. 12(a). The location of upper TZ frequencies (f_{z2} and f_{z3}) are shifted towards the left with increasing power level for greater values of r. This phenomenon allows regulation of the BW (TB and Stopband towards lower frequencies) and selectivity simply by adjusting r.

In Fig. 12(b), when the inner circle radius (s) is improved from 0.18 mm to 0.26 mm, the position of f_{z2} and f_{z3} switches towards lower frequencies. Thus, the BW of TB along with the upper stopband can be controlled by s.

So, after performing a parametric analysis of the proposed filter, we can figure out which parameter affects the filter's properties. At least one of the filter properties, such as return loss, insertion loss, placements, and power level of RP frequencies, and TZ frequencies, are affected by one of the design

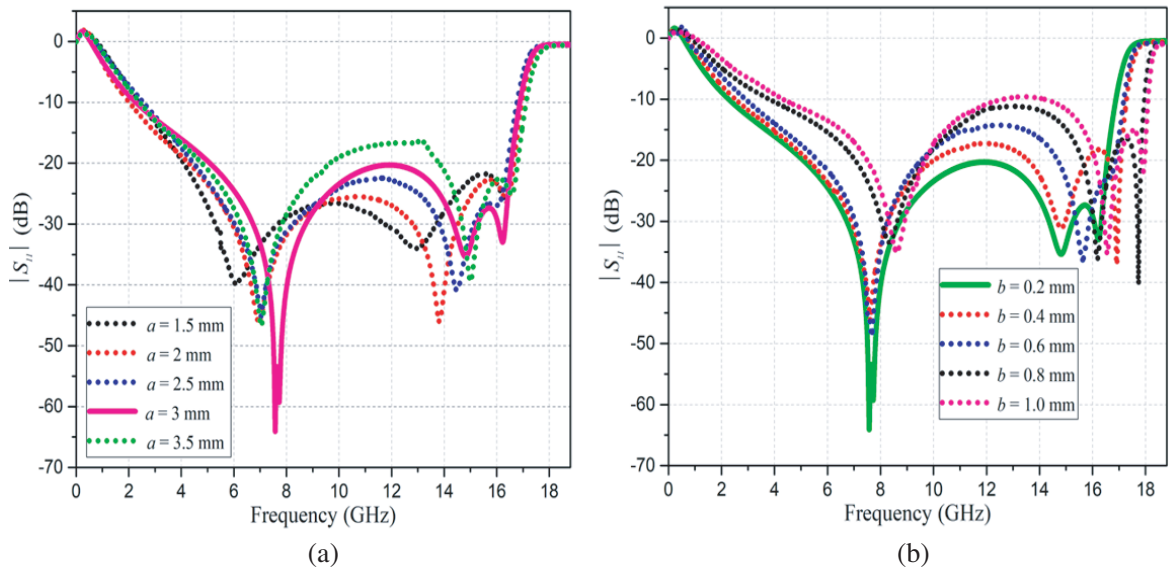

Figure 11. Magnitude of S_{11} for different (a) a, (b) b.

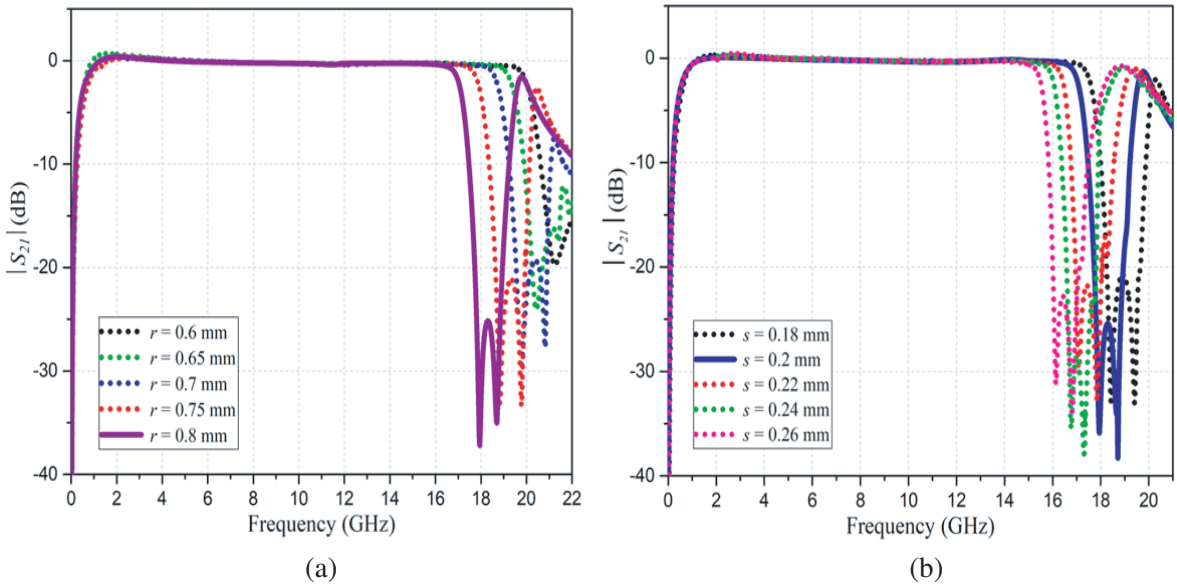

Figure 12. Magnitude of S_{21} for varying (a) r, (b) s.

parameters of the filter. The optimized filter parameters in the S-parameter plot can be identified by solid lines among dotted lines.

6. FABRICATED FILTER

To validate the simulated and analytical results, the proposed filter is fabricated and tested. Fig. 13(a) and Fig. 13(b) depict the top and bottom views of the fabricated model, respectively. Using a Vector Network Analyzer (VNA), the filter response is experimentally validated after calibration. Measured (solid lines) and simulated (dotted lines) S-parameter curves are shown in Fig. 14. From VNA the reflection loss and insertion loss are 18.5 dB and 0.72 dB, respectively, encompassing a frequency range

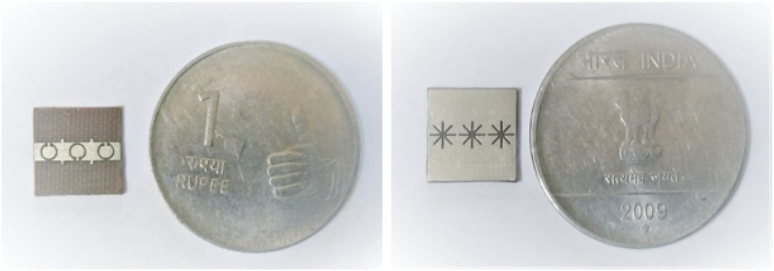

(a) (b)

Figure 13. Photograph of fabricated model of presented filter. (a) Top view. (a) Bottom view.

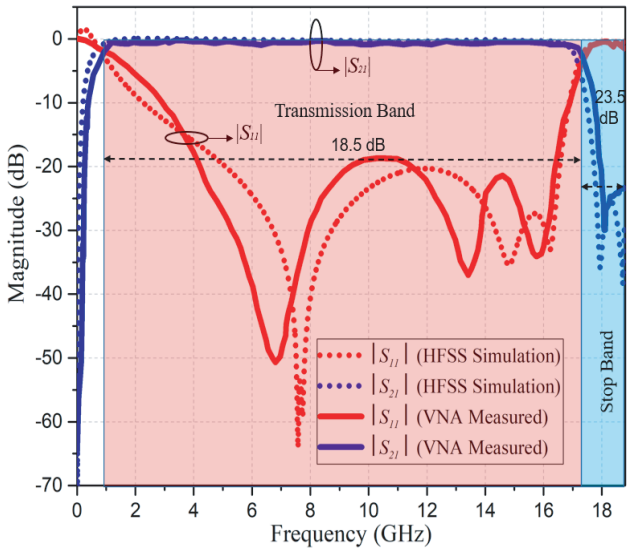

Figure 14. Comparison diagram of filter performance in terms of magnitude of S-parameters by EM simulation and VNA.

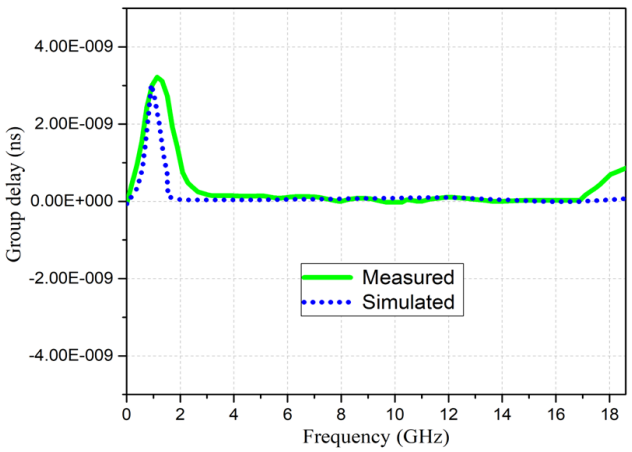

Figure 15. Group delay of the proposed filter in EM simulation and VNA.

of 0.8 GHz to 17.4 GHz (TB) at a 3 dB level. Two TZs and three RPs are observed at 0 GHz, 18.1 GHz, 6.84 GHz, 13.4 GHz, and 15.8 GHz, respectively. Also, the upper stopband region is suppressed about 23.5 dB from 18.15 GHz to 18.8 GHz. A slight deviation of VNA results from EM simulation is a consequence of fabrication tolerances and connector loss.

Figure 15 reveals the group delay of the UBB BPF that varies from 0 ns to 2.95 ns in HFSS simulation represented by a dotted line. In the case of a VNA, the maximum group delay of the filter within the frequency range (0 GHz to 18.8 GHz) is about 3.35 ns indicated by a solid line. Indeed, the group delay of the filter is less and flat since the lower order and wider BW nature of the UBB BPF. A minimum (flat) group delay is observed over the TB of the filter. Because of the tolerances in the fabrication process and connector loss, the obtained results are slightly different from the ones that were simulated. The limitation of this work lies in the lower stopband region of the filter which is not much attenuated.

Table 2 provides a comparison of various filters with the proposed filter. The size of the proposed BPF seems compact compared to BPFs in [23–29]. The BW of existing filters in [23–29] is less than 16.6 GHz compared to the proposed BPF. Though insertion loss is better (less than 0.72 dB) in [27, 28], and around 3 dB insertion loss is observed in [29]. Indeed cost-effective BPFs are not feasible with multiple substrates as in [23, 26–28]. Thus, the proposed BPF shows a better performance in terms of size, insertion loss, passband, and the number of substrates than existing BPFs.

Table 2. Comparison of existing bandpass filter with the proposed filter

Ref.	Size (mm $*$ mm)	Insertion Loss (dB)	Number of Substrates	TB (GHz)
[23]	$87.5 * 12.8$	1.1	2	0.25–4.5
[24]	$\sim 47 * 24$	(NA)	1	3.25–6.05
[25]	$302 * 302$	1	None	8.76–11.96
[26]	$36.2 * 11.7$	< 0.75	2	1.57–6.51
[27]	$21.95 * 16.46$	0.42	2	2.56–11.15
[28]	$20.8 * 20$	0.58	3	10.215–15.375
[29]	$60 * 40$	3	1	2.9–16.2
Proposed	$10 * 10$	0.72	1	0.8–17.4

7. CONCLUSION

A miniaturized third-order UBB BPF using novel DMS and DGS resonators with an FBW of 178.5% was designed and fabricated on a low-loss Taconic substrate. Using transmission line model analysis, the $ABCD$ matrix was used to validate the S-parameters concerning EM simulation response. The configuration and shape of DMS, DGS, and OC stubs result in better coupling of electric and magnetic fields between resonators and among layers which was well illustrated. The performance of the filter has been investigated by parametric analysis and achieved an optimized filter. The equivalent circuit of the novel filter was constructed using lumped elements, and the results were compared with the EM simulation which had good agreement with each other. Finally, the prototype of the filter was tested with the help of a VNA, and thus the filter was able to provide transmission from 0.8 GHz to 17.4 GHz with 16.6 GHz 3 dB BW. The sample filter measured 18 dB return loss, 0 dB to 0.72 dB insertion loss inside the TB, and 23.5 dB attenuation in the upper stopband BW of 0.65 GHz. The measured group delay of the presented BPF was 3.35 ns inside the TB. Since the BPF covers L, S, C, X, and Ku frequency bands, it is applicable to mobile phones and satellite communication applications.

REFERENCES

1. Min, B. C., Y. H. Choi, S. K. Kim, and B. Oh, "Cross-coupled band-pass filter using HTS microstrip resonators," *IEEE Trans. Appl. Supercond.*, Vol. 11, No. 1, 485–488, 2001.
2. Bonache, J., I. Gil, J. Garcia-Garcia, and F. Martin, "Novel microstrip bandpass filters based on complementary split-ring resonators," *IEEE Trans. Microw. Theory Tech.*, Vol. 54, No. 1, 265–271, 2006.
3. Wu, B., C. H. Liang, P. Y. Qin, and Q. Li, "Compact dual-band filter using defected stepped impedance resonator," *IEEE Microw. Wirel. Compon. Lett.*, Vol. 18, No. 10, 674–676, 2008.
4. Sun, S., "A dual-band bandpass filter using a single dual-mode ring resonator," *IEEE Microw. Wirel. Compon. Lett.*, Vol. 21, No. 6, 298–300, 2011.
5. Shen, W., W. Y. Yin, X. W. Sun, and L. S. Wu, "Substrate-integrated waveguide bandpass filters with planar resonators for system-on-package," *IEEE Trans. Compon. Packag. Manuf. Technol.*, Vol. 3, No. 2, 253–261, 2012.
6. Park, J. S., J. S. Yun, and D. Ahn, "A design of the novel coupled-line bandpass filter using defected ground structure with wide stopband performance," *IEEE Trans. Microw. Theory Tech.*, Vol. 50, No. 9, 2037–2043, 2002.
7. Abdel-Rahman, A., A. K. Verma, A. Boutejdar, and A. S. Omar, "Compact stub type microstrip bandpass filter using defected ground plane," *IEEE Microw. Wirel. Compon. Lett.*, Vol. 14, No. 4, 136–138, 2004.

8. Tan, B. T., J. J. Yu, S. T. Chew, M. S. Leong, and B. L. Ooi, "A miniaturized dual-mode ring bandpass filter with a new perturbation," *IEEE Microw. Wirel. Compon. Lett.*, Vol. 53, No. 1, 343–348, 2005.
9. El-Shaarawy, H. B., F. Coccetti, R. Plana, M. El Said, and E. A. Hashish, "Compact bandpass ring resonator filter with enhanced wide-band rejection characteristics using defected ground structures," *IEEE Microw. Wirel. Compon. Lett.*, Vol. 18, No. 8, 500–502, 2008.
10. Hamad, E. K., A. M. Safwat, and A. S. Omar, "Controlled capacitance and inductance behaviour of L-shaped defected ground structure for coplanar waveguide," *IEE Proc.: Microw., Antennas and Prop.*, Vol. 152, No. 5, 299–304, 2005.
11. Lee, J. K. and Y. S. Kim, "Ultra-wideband bandpass filter with improved upper stopband performance using defected ground structure," *IEEE Microw. Wirel. Compon. Lett.*, Vol. 20, No. 6, 316–318, 2010.
12. Zhou, J., Y. Rao, D. Yang, H. J. Qian, and X. Luo, "Compact wideband BPF with wide stopband using substrate integrated defected ground structure," *IEEE Microw. Wirel. Compon. Lett.*, Vol. 31, No. 4, 353–356, 2021.
13. Wang, C., X. Zhang, T. Xia, Y. Zhang, and Q. Fan, "Dual-band filter power divider with controllable transmission zero based on multimode resonator," *Progress In Electromagnetics Research Letters*, Vol. 105, 9–16, 2022.
14. Tu, W. H., "Compact low-loss reconfigurable bandpass filter with switchable bandwidth," *IEEE Microw. Wirel. Compon. Lett.*, Vol. 20, No. 4, 208–210, 2010.
15. Hou, Z. J., Y. Yang, X. Zhu, Y. C. Li, E., Dutkiewicz, and Q. Xue, "A compact and low-loss bandpass filter using self-coupled folded-line resonator with capacitive feeding technique," *IEEE Electron Device Lett.*, Vol. 39, No. 10, 1584–1587, 2018.
16. Wang, Z., J. Ma, S. Zhao, H. Liu, and S. Fang, "A novel DGS-based substrate integrated coaxial line bandpass filter with three transmission zeros," *Progress In Electromagnetics Research Letters*, Vol. 105, 1–8, 2022.
17. Tirado-Mendez, J. A., H. Jardon-Aguilar, R. Flores-Leal, E. Andrade-Gonzalez, and F. Iturbide-Sanchez, "Improving frequency response of microstrip filters using defected ground and defected microstrip structures," *Progress In Electromagnetics Research C*, Vol. 13, 77–90, 2010.
18. Hanae, E., N. A. Touhami, and M. Aghoutane, "Miniaturized microstrip patch antenna with spiral defected microstrip structure," *Progress In Electromagnetics Research Letters*, Vol. 53, 37–44, 2015.
19. Elftouh, H., N. A. Touhami, M. Aghoutane, S. El Amrani, A. Tazón Puente, and M. Boussouis, "Miniaturized microstrip patch antenna with defected ground structure," *Progress In Electromagnetics Research C*, Vol. 55, 25–33, 2014.
20. Hong, J. S. G. and M. J. Lancaster, *Microstrip Filters for RF/Microwave Applications*, John Wiley & Sons, Hoboken, 2004.
21. Kim, C. S., J. S. Park, D. Ahn, and J. B. Lim, "A novel 1-D periodic defected ground structure for planar circuits," *IEEE Microw. and Guided Wave Lett.*, Vol. 10, No. 4, 131–133, 2000.
22. Weng, L. H., Y. C. Guo, X. W. Shi, and X. Q. Chen, "An overview on defected ground structure," *Progress In Electromagnetics Research B*, Vol. 7, 173–189, 2008.
23. Wang, M., S. Sun, H. F. Ma, and T. J. Cui, "Supercompact and ultrawideband surface plasmonic bandpass filter," *IEEE Trans. Microw. Theory Tech.*, Vol. 68, No. 2, 732–740, 2019.
24. Bandyopadhyay, A., P. Sarkar, and R. Ghatak, "A bandwidth reconfigurable bandpass filter for ultrawideband and wideband applications," *IEEE Trans. Circuits Syst. II Express Briefs*, Vol. 69, No. 6, 2747–2751, 2022.
25. Lalbakhsh, A., M. U. Afzal, K. P. Esselle, and S. L. Smith, "All-metal wideband frequency-selective surface bandpass filter for TE and TM polarizations," *EEE Trans. Antennas Propag.*, Vol. 70, No. 4, 2790–2800, 2022.
26. Zhang, T., M. Tian, Z. Long, M. Qiao, and Z. Fu, "High-temperature superconducting multimode ring resonator ultrawideband bandpass filter," *IEEE Microw. Wirel. Compon. Lett.*, Vol. 28, No. 8, 663–665, 2018.

27. Long, Z., M. Tian, T. Zhang, M. Qiao, T. Wu, and Y. Lan, "High-temperature superconducting multimode dual-ring UWB bandpass filter," *IEEE Trans. Appl. Supercond.*, Vol. 30, No. 2, 1–4, 2019.
28. Li, C., Z. H. Ma, J. X. Chen, M. N. Wang, and J. M. Huang, "Design of a compact ultra-wideband microstrip bandpass filter," *Electronics*, Vol. 12, No. 7, 1728, 2023.
29. Lin, D. B., M. H. Wang, A. A. Pramudita, and T. Adiprabowo, "Design of a novel ultra-wideband common-mode filter using a magnified coupled defected ground structure," *Appl. Sci.*, Vol. 13, No. 13, 7404, 2023.